Nanostructures

DOI: 10.1002/anie.201406468

Surface Polarization Matters: Enhancing the Hydrogen-Evolution Reaction by Shrinking Pt Shells in Pt–Pd–Graphene Stack Structures**

*Song Bai, Chengming Wang, Mingsen Deng, Ming Gong, Yu Bai, Jun Jiang, and Yujie Xiong**

Abstract: *Surface charge state plays an important role in tuning the catalytic performance of nanocrystals in various reactions. Herein, we report a synthetic approach to unique Pt–Pd–graphene stack structures with controllable Pt shell thickness. These unique hybrid structures allow us to correlate the Pt thickness with performance in the hydrogen-evolution reaction (HER). The HER activity increases with a decrease in the Pt thickness, which is well explained by surface polarization mechanism as suggested by first-principles simulations. In this hybrid system, the difference in work functions of Pt and Pd results in surface polarization on the Pt surface, tuning its charge state for hydrogen reduction. Meanwhile, the supporting graphene provides two-dimensional channels for efficient charge transport, improving the HER activities. This work opens up possibilities of reducing Pt usage while achieving high HER performance.*

To meet the increasing energy and environmental demands, various approaches have been developed to produce hydrogen—an energy source with high energy density and minimal pollution. The electrocatalytic hydrogen-evolution reaction (HER, $2H^+ + 2e^- \rightarrow H_2$) represents a highly important process for hydrogen generation, for reversible hydrogen fuel-cell technology.[1,2] Despite tremendous efforts to find alternative materials,[3,4] Pt is still the most efficient electrocatalyst for the HER.[5–7] Even compared with other noble metals, such as Pd, the Pt typically shows lower overpotential and higher current density. Nevertheless, decreasing the Pt usage is always the ultimate goal for electrocatalysts design to achieve cost-effective hydrogen production.

Towards this goal, an open question remains: can the HER performance be boosted when the Pt amount is decreased in the catalysts? If accomplished, it would provide an ideal solution to the HER catalysts with both high performance and low cost. In other electrocatalytic systems, various approaches have be tried; it has been attempted to dope graphene with nitrogen which turns out to show enhanced activities in oxygen reduction reaction (ORR) as a result of the electronegativity different between N and C.[8,9] These results highlight the importance of the surface charge state for electrocatalytic reactions.[10] To tailor the Pt surface charge, we thus decided to take advantage of surface polarization, an effect that has been occasionally demonstrated for tuning catalysis. This surface polarization is mostly induced by an external electric field or by ferroelectric substrates.[11,12]

Herein, we report that the surface polarization enabled by the difference in the work function between Pt and Pd can boost the HER performance of Pt surface, based on a Pt–Pd–rGO (reduced graphene oxide) stack structure. It is a unique approach to cost-effective, high-performance catalyst design because the Pt thickness required in this structure is just a few atomic layers to ensure the polarization, providing the possibilities of decreasing Pt usage. We have intentionally made some adjustments for this Pt–Pd–rGO stack design: 1) {100} facets are selected for Pd and Pt, as they not only offer a flat surface for contact with the graphene substrates but have relatively high current density (J) in HER;[7] 2) deposition of Pt–Pd nanocrystals on rGO, as the rGO can facilitate charge transfer and ionic interchange to enhance electrocatalysis (also demonstrated in our characterizations, Supporting Information Figure S1–S4).[13–15]

Our Pt–Pd–rGO nanostructures are synthesized by a two-step process. As illustrated in Figure 1a, Pd nanocubes are grown in situ on the rGO sheets by co-reducing K_2PdCl_4 and graphene oxide (GO) nanosheets with ascorbic acid. From transmission electron microscopy (TEM) images (Figure S1a and S1b), it can be seen that the Pd nanocrystals deposited on the rGO sheets have a well-defined cubic profile with an edge length of approximately 12 nm. High-resolution TEM (HRTEM) images (Figure S1c) further confirm that the cubic nanocrystals are single crystals enclosed by Pd {100} facets.

In the next step, we selectively coat Pt shells onto the Pd nanocrystals by reducing H_2PtCl_6 in *N*,*N*-dimethylformamide (DMF). As shown in Figure 1b,c and Figure S5, a number of cubic nanocrystals are dispersed on rGO sheets. According to

[*] S. Bai,[+] Dr. C. Wang,[+] Dr. M. Deng,[+] Prof. M. Gong, Y. Bai, Prof. J. Jiang, Prof. Y. Xiong
Hefei National Laboratory for Physical Sciences at the Microscale
Collaborative Innovation Center of Chemistry for Energy Materials
School of Chemistry and Materials Science, and Laboratory of Engineering and Material Science, University of Science and Technology of China
Hefei, Anhui 230026 (P. R. China)
E-mail: yjxiong@ustc.edu.cn
Homepage: http://staff.ustc.edu.cn/~yjxiong/
Dr. M. Deng[+]
Guizhou Provincial Key Laboratory of Computational Nano-Material Science, Guizhou Normal College
Guiyang, Guizhou 550018 (P. R. China)

[+] These authors contributed equally to this work.

[**] This work was financially supported by 973 Program (No. 2014CB848900), NSFC (No. 21101145, 91123010, 21203037), Hok Ying Tung Education Foundation (No. 131012), Recruitment Program of Global Experts, CAS Hundred Talent Program, and Construction Project for Guizhou Provincial Key Laboratories (ZJ20114007).

Supporting information (materials synthesis, sample characterizations, electrochemical characterizations, and computational methods) for this article is available on the WWW under http://dx.doi.org/10.1002/anie.201406468.

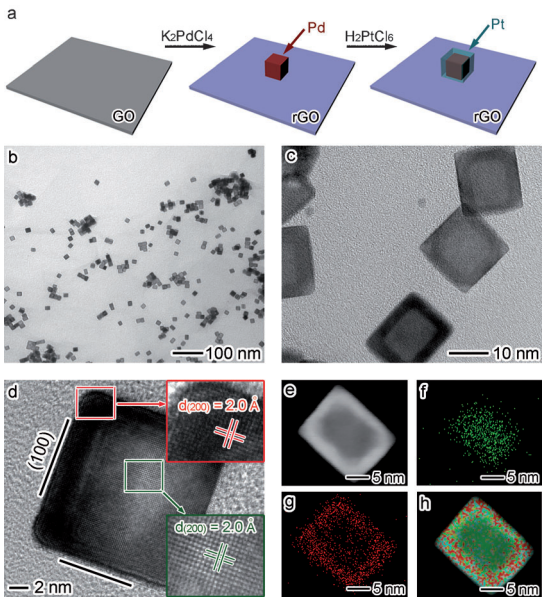

Figure 1. a) Schematic illustration for the synthesis of Pt–Pd–rGO structures. b,c) TEM images of the Pt–Pd–rGO structure (namely Pt–Pd–rGO II). d) HRTEM image of a Pt–Pd nanocrystal on the rGO. e) STEM image and f–h) EDS mapping profiles of a single Pt–Pd nanocrystal on the rGO, element profiles for f) Pd (green), g) Pt (red), and h) Pt–Pd-STEM overlay.

the image contrast, it seems that the nanocrystals are core–shell structures with an average shell thickness of about 2 nm (namely, Pt–Pd–rGO II). The HRTEM image in Figure 1 d reveals that the shell is a piece of single crystal enclosed by {100} facets, forming perfect interface with the existing single-crystal Pd nanocrystal (i.e., core) in the Pd–rGO precursor. Although the meticulous lattice mismatch between Pd and Pt cannot be well distinguished by the lattice fringes, scanning TEM (STEM) image, together with their energy-dispersive spectroscopy (EDS) mapping analyses (Figure 1 e–h), further confirm the elemental distributions in the hybrid structures. The EDS mapping clearly displays that Pt and Pd are enriched in the shells and cores, respectively (see also Figure S6). Notably, as compared with the reported Pd–Pt core–shell structures,[16] the image contrast between the Pd core and Pt shell in our hybrid structures is significantly higher, as the structures presented herein are not truly "core–shell". In our Pt–Pd–rGO stack structures, the bottom surface of Pd nanocubes is in contact with the rGO and thus not covered by Pt, making the Pd signal more dominant in the central region during imaging. The phases and compositions of Pt–Pd–rGO structures are further verified by X-ray diffraction (XRD, Figure S7) and X-ray photoelectron spectroscopy (XPS, Figure S8). The XPS data show that most O-containing functional groups have been removed from the rGO sheets during their reduction by ascorbic acid and DMF (see detailed analysis for Pd and Pt in Supporting Information).[17,18] Thus, the in situ growth of Pd on rGO as well as the epitaxial growth of Pt on Pd have formed high-quality Pd–rGO and Pt–Pd interfaces in our ternary stack structures, ensuring efficient charge transport.

Table 1: Pt/Pd molar ratio and estimated average Pt shell thickness for different Pt–Pd–rGO samples. The Pt/Pd ratio is determined by ICP-MS.

Samples	Pt/Pd molar ratio	Estimated average Pt shell thickness [nm]
Pt–Pd–rGO I	0.41	0.8
Pt–Pd–rGO II	0.94	1.8
Pt–Pd–rGO III	1.94	3.2

Interestingly, the thickness of Pt shells can be controlled by simply altering the ratio of rGO–Pd to Pt precursor in our synthetic scheme. Decreasing the amount of rGO–Pd suspension from 4.0 to 1.0 mL (see synthetic method in Supporting Information), we have been able to tune the Pt shell thickness from 0.8 to 3.2 nm (Table 1) as determined by inductively coupled plasma mass spectrometry (ICP-MS). Naturally, this increasing thickness increases the lateral dimensions as shown in the TEM images (Figure 2, also see

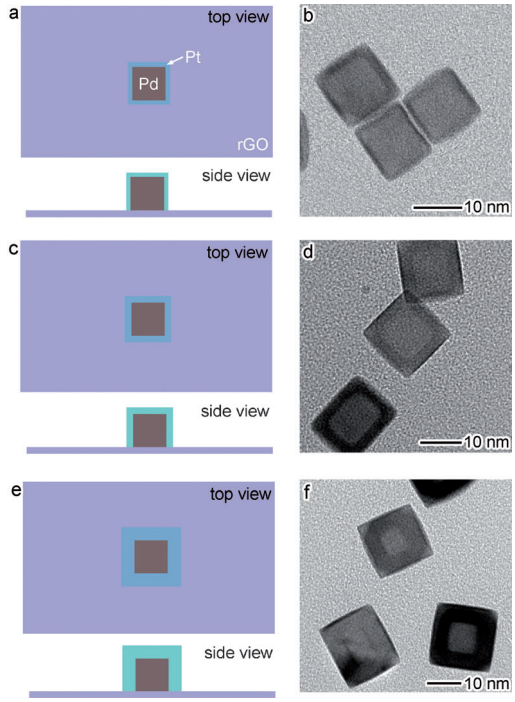

Figure 2. Schematic illustrations and TEM images for a,b) Pt–Pd–rGO I; c,d) Pt–Pd–rGO II; and e,f) Pt–Pd–rGO III hybrid structures with tunable Pt thickness.

size distributions in Figure S9). We name this series of ternary hybrid structures as Pt–Pd–rGO I, II, and III with the increase of Pt shell thickness (Figure 1, and Figures S10, S11). From the change from I to III, it can be seen that the image contrast between Pt and Pd increases first but tends to diminish once the Pt becomes dominant in the structures, this is a result of the higher electron density of Pt than Pd. While the Pd cores in Pt–Pd–rGO III are unapparent in TEM images they are clearly are identified by EDS characterizations (Figure S11), tremendous Pt deposition causes notable differences between the lateral lengths and height of Pt shells as one Pd face is blocked by rGO. Figure S12 shows a TEM image of the

nanocrystals in Pt–Pd–rGO III sample with varied orientations relative to the electron beam, clearly showing this difference.

Upon achieving the controllable synthesis, we are in a position to investigate why Pt can be selectively deposited on Pd nanocubes rather than on rGO sheets. To elucidate the underlying mechanism, we first perform a control experiment using bare Pd nanocubes (Figure S2a) instead of Pd–rGO as precursors. It turns out that the Pt cannot be grow on the Pd nanocubes to form Pd–Pt "core–shell" structures (Figure S13), implying that the rGO plays an important role in the growth of Pt on Pd. Assuming that the interface of Pd–rGO is indispensable for the selective growth, we have analyzed the reduction potentials of rGO and metal species. As listed in Table S1,[19,20] the potential difference between rGO and Pd causes electrons to accumulate on the Pd surface (Figure S14). In the synthesis of Pt–Pd–rGO structures, the heterogeneous electron distribution means that the Pt is preferentially reduced on the Pd surface which has a relatively high electron density. Given the higher potential of Pt ($PtCl_6^{2-}$/Pt + 0.74 V vs. SHE) than Pd ($PdCl_4^{2-}$/Pd + 0.62 V vs. SHE) (SHE: standard hydrogen electrode),[21] the reaction in Equation (1) may take place at the initial stage:

$$2\,Pd_{(s)} + PtCl_6^{2-}{}_{(sol)} + 2\,Cl^-{}_{(sol)} \rightarrow Pt_{(s)} + 2\,PdCl_4^{2-}{}_{(sol)} \quad (1)$$

The initial deposition of trace amounts of Pt on the Pd nanocubes can provide active sites to induce further Pt growth. In the redox reactions, the Pd atoms would not be oxidized and dissolved away, as the rGO with potential of + 0.38 V vs. SHE can provide a steady electron supply to prevent the oxidation of Pd. This working mechanism is analogous to the underpotential deposition (UPD) process.[22–24]

To confirm the mechanism, we have applied this synthetic scheme to other noble metals with different reduction potentials. When the $HAuCl_4$ is used in the synthesis, Au shells can also selectively grow on the Pd surface of Pd–rGO (Figure S15), simply because of the high potential of Au ($AuCl_4^-$/Au + 1.002 V vs. SHE). In sharp contrast, the growth of Ag nanocrystals occurs at the rGO instead of on the Pd surface (Figure S16a,b), as $AgNO_3$ is employed as the metal source. In the absence of chloride in the reactions, the reduction potential of Ag (Ag^+/Ag + 0.7996 V vs. SHE) is more negative than that of Pd (Pd^{2+}/Pd + 0.951 V vs. SHE) so the Ag cannot be reduced on the Pd surface. Note that Pd–Ag core–shell structures can be formed when the Ag growth is conducted through the same method as ours except using bare Pd nanocubes instead of Pd–rGO.[25] Following the same mechanism (Ru^{3+}/Ru + 0.386 V vs. SHE), Ru is also deposited at the rGO rather than on the Pd when $RuCl_3$ is used as a precursor (Figure S16c,d). It suggests that the potential difference between the rGO, Pd, and the deposition metal in sequence is the key to achieving our synthesis.

This controllable synthesis offers an ideal platform for the HER studies. Prior to the measurements, the sample surface is cleaned through oxygen plasma and hundreds of potential cycles till the cyclic voltammetry curves (CVs) stay unchanged and exhibit well-resolved Pt peaks, to ensure residual organics and ions are released. We first compare our Pt–Pd–rGO III sample with the Pt-rGO hybrid structures (with the same Pt(100) surface, Figure S3) and commercial Pt/C catalysts on glassy carbon rotating disk electrodes in a 0.5 M H_2SO_4(aq) electrolyte. The total metal loading weights are kept constant for this assessment. The polarization curves of the current density plotted against potential (Figure S17a) show that the activities of Pt–Pd–rGO III and Pt–rGO samples are higher than that of Pt/C, as the Pt(100) has a superior HER activity to Pt(111).[7] Interestingly, our Pt–Pd–rGO III sample with thick Pt shells exhibits comparable HER performance to the Pt–rGO in terms of both the current densities and Tafel slopes (Figure S17b). It indicates that the ternary stack structures mainly reflect the intrinsic property of Pt(100) in HER when the shells are thick enough.

Given the Pt(100) behavior of Pt–Pd–rGO III sample, we further examine the effect of Pt thickness on the HER performance. In this evaluation, we intentionally maintain the same Pd loading amounts for all the three samples so that the Pt thickness effect can be better resolved. In this case, the number of Pt–Pd nanocrystals is kept constant for all the samples, and the surface areas of the samples follow the sequence Pt–Pd–rGO I < Pt–Pd–rGO II < Pt–Pd–rGO III. Strikingly, the current densities at the same potential are found to be in the order Pt–Pd–rGO I > Pt–Pd–rGO II > Pt–Pd–rGO III with a near zero overpotential (Figure 3a), despite the significantly decreased total metal loading amounts and surface areas going from samples III to I. Note that the total metal loading weight of the Pt–Pd–rGO III sample is kept consistent with that for the comparison in Figure S17. Both the Tafel slopes and overpotentials are in

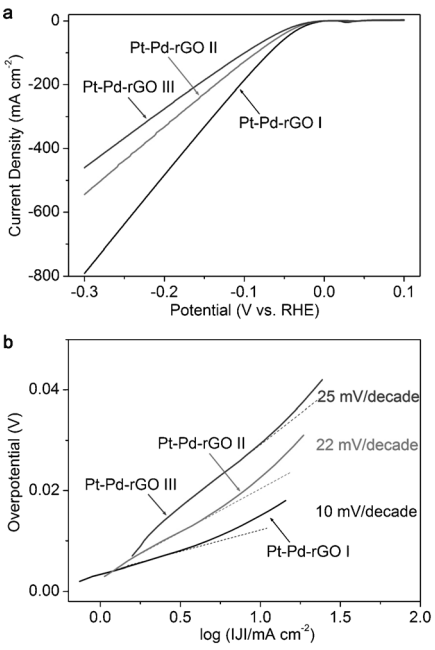

Figure 3. a) Polarization curves obtained on glassy carbon rotating disk electrodes coated with Pt–Pd–rGO structures which have different Pt thickness at equal Pd loading amounts. The total metal loading weight of Pt–Pd–rGO III is consistent with that in Figure S17. b) The corresponding Tafel plots. The dashed lines indicate the linear regions.

inverse order, also demonstrating that the HER performance is enhanced with Pt thickness reduction. Of the samples, the Pt–Pd–rGO I with the thinnest Pt shell shows the highest activity with an extremely large current density of 791 mA cm^{-2} at a potential of −300 mV, and its calculated Tafel slope of 10 mV decade^{-1} is among the lowest reported for HER electrocatalysts. The electrochemical stability of the samples is also measured by running continuous CVs between −0.3 and 0.1 V vs. RHE at 50 mV s^{-1} (RHE = reversible hydrogen electrode). Negligible decay in the HER activity can be observed between the curves measured at the initial cycle and after 5000 cyclic voltammetry (CV) cycles, suggesting the excellent durability of Pt–Pd–rGO samples during long-term cycling (Figure S18).

It is natural to ask what factor is responsible for this thickness-dependent HER performance? To decode the underlying mechanism, we have employed first-principles simulations to examine the interface between Pd and Pt.[26] The computed work functions of Pd{100} and Pt{100} are 5.14 and 5.68 eV, respectively, suggesting a flow of electrons from Pd to Pt so as to equilibrate the electron Fermi distribution at the their interface. As indicated by the differential charge density (Figure 4), distinct interfacial polarization occurs when the Pt atoms are of 1–2 atomic layers, resulting in substantial negative charges (Figure 4, olive color) on the Pt surface. For the HER ($2H^+ + 2e^- \rightarrow H_2$), the increase of electron density on the catalyst surface surely improves the reaction activity. As the Pt thickness reaches 4 atomic layers, the surface polarization effect becomes much weaker. In fact, from the HER performance the most distinct difference comes from the Pt–Pd–rGO I and Pt–Pd–rGO II samples (i.e., roughly the borderline of 4 atomic layers; Figure 3). The current density of Pt–Pd–rGO II is 247 mA cm^{-2} lower than the sample I at potential of −300 mV, and its Tafel slopes is beyond two-times larger. In stark contrast, the HER performance variation becomes indistinct when the Pt thickness is further increased from the sample II to III, implying the significantly weakened polarization effect. It should be noted that the simulations herein focus on the static polarization effect and therefore mainly reflect a trend of surface polarization along with the Pt thickness. In the practical HER reaction, dynamic charge distribution may make the polarization effect impact beyond the 4th Pt layer.

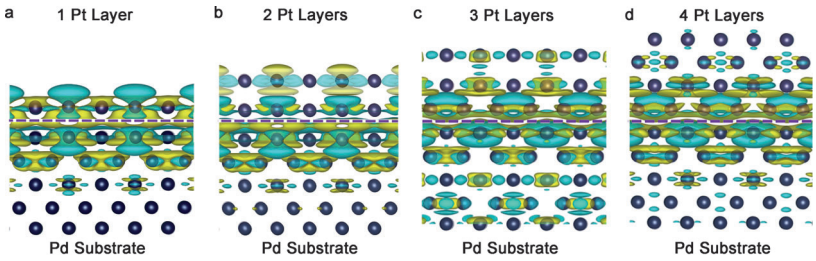

Figure 4. Differential charge density by first-principles simulations illustrating the alterations of electron distributions with the Pt thickness: a) 1 layer, 2) 2 layers, c) 3 layers, and d) 4 layers. The olive and cyan represent increase and decrease in electron density, respectively. In the simulations, Pd substrates are covered by various layers of Pt atoms to assess the dependence of surface polarization on Pt thickness. The simulation models are shown in Figure S20.

Simulations also reveal that graphene has a strong electronic coupling with Pd and Pt according to their highly hybridized projected density of state (PDOS; Figure S19), thus acting as an electron source to ensure the HER reaction. In our measurements, the rGO promotes the HER performance regardless of whether Pd or Pt is supported (Figure S4), as it can help prevent the aggregation of metal nanocrystals and provide interconnected and resistance-less network for efficient catalyst-electrode electron transfer.[13–15] In our stack structures, both the Pt–Pd surface polarization and rGO supports make important contributions to improving the HER performance.

In summary, we have developed a unique synthetic approach to prepare Pt–Pd–rGO stack structures with controllable Pt shell thickness. The HER performance of these hybrid structures turns out to have a strong correlation with the shell thickness, in accord with a surface polarization mechanism. By substantially reducing the Pt thickness, we obtain a sample with current density up to 791 mA cm^{-2} at potential of −300 mV and Tafel slope as low as 10 mV decade^{-1}, achieving impressive HER performance. This surface polarization mechanism requiring low shell thickness opens up new possibilities of reducing the usage of expensive Pt. We envision that it would provide fresh insights into rationally designing the hybrid catalysts from a different perspective. It is anticipated that this strategy combined with the atomic layer deposition (ALD) technique offering single-layer Pt deposition would enable further enhanced catalytic performance with minimal usage of Pt.

Received: June 22, 2014
Published online: August 26, 2014

Keywords: hybrid structures · hydrogen-evolution reaction · nanocrystals · surface polarization · work function

[1] C. G. Morales-Guio, L. A. Stern, X. Hu, *Chem. Soc. Rev.* **2014**, *43*, 6555.
[2] W. F. Chen, J. T. Muckerman, E. Fujita, *Chem. Commun.* **2013**, *49*, 8896.
[3] H. I. Karunadasa, E. Montalvo, Y. Sun, M. Majda, J. R. Long, C. J. Chang, *Science* **2012**, *335*, 698.
[4] L. Cheng, W. Huang, Q. Gong, C. Liu, Z. Liu, Y. Li, H. Dai, *Angew. Chem. Int. Ed.* **2014**, *53*, 7860; *Angew. Chem.* **2014**, *126*, 7994.
[5] X. Huang, Z. Zeng, S. Bao, M. Wang, X. Qi, Z. Fan, H. Zhang, *Nat. Commun.* **2013**, *4*, 1444.
[6] D. V. Esposito, S. T. Hunt, A. L. Stottlemyer, K. D. Dobson, B. E. McCandless, R. W. Birkmire, J. G. Chen, *Angew. Chem. Int. Ed.* **2010**, *49*, 9859; *Angew. Chem.* **2010**, *122*, 10055.
[7] N. M. Marković, B. N. Grgur, P. N. Ross, *J. Phys. Chem. B* **1997**, *101*, 5405.
[8] L. Qu, Y. Liu, J. B. Baek, L. Dai, *ACS Nano* **2010**, *4*, 1321.

[9] X. K. Kong, C. L. Chen, Q. W. Chen, *Chem. Soc. Rev.* **2014**, *43*, 2841.
[10] Y. Zheng, Y. Jiao, L. H. Li, T. Xing, Y. Chen, M. Jaroniec, S. Z. Qiao, *ACS Nano* **2014**, *8*, 5290.
[11] A. M. Kolpak, I. Grinberg, A. M. Rappe, *Phys. Rev. Lett.* **2007**, *98*, 166101.
[12] C. G. Vayenas, S. Bebelis, S. Ladas, *Nature* **1990**, *343*, 625.
[13] Y. Zheng, Y. Jiao, Y. Zhu, L. H. Li, Y. Han, Y. Chen, A. Du, M. Jaroniec, S. Z. Qiao, *Nat. Commun.* **2014**, *5*, 3783.
[14] Y. Li, H. Wang, L. Xie, Y. Liang, G. Hong, H. Dai, *J. Am. Chem. Soc.* **2011**, *133*, 7296.
[15] C. Wang, L. Ma, L. Liao, S. Bai, R. Long, M. Zuo, Y. Xiong, *Sci. Rep.* **2013**, *3*, 2580.
[16] M. Shao, G. He, A. Peles, J. H. Odell, J. Zeng, D. Su, J. Tao, T. Yu, Y. Zhu, Y. Xia, *Chem. Commun.* **2013**, *49*, 9030.
[17] B. Y. Xia, B. Wang, H. B. Wu, Z. Liu, X. Wang, X. W. Lou, *J. Mater. Chem.* **2012**, *22*, 16499.
[18] C. Hsu, C. Huang, Y. Hao, F. Liu, *Electrochem. Commun.* **2012**, *23*, 133.
[19] B. Kong, J. Geng, H. Jung, *Chem. Commun.* **2009**, 2174.
[20] R. C. Weast, *Handbook of Chemistry and Physics*, CRC, Boca Raton, FL, **1980**.
[21] H. Zhang, M. Jin, J. Wang, W. Li, P. H. C. Camargo, M. J. Kim, D. Yang, Z. Xie, Y. Xia, *J. Am. Chem. Soc.* **2011**, *133*, 6078.
[22] Y. Yu, Q. Zhang, J. Xie, J. Y. Lee, *Nat. Commun.* **2013**, *4*, 1454.
[23] M. L. Personick, M. R. Langille, J. Zhang, C. A. Mirkin, *Nano Lett.* **2011**, *11*, 3394.
[24] A. R. Tao, P. Sinsermsuksakul, P. Yang, *Angew. Chem. Int. Ed.* **2006**, *45*, 4597; *Angew. Chem.* **2006**, *118*, 4713.
[25] J. Zeng, C. Zhu, J. Tao, M. Jin, H. Zhang, Z. Y. Li, Y. Zhu, Y. Xia, *Angew. Chem. Int. Ed.* **2012**, *51*, 2354; *Angew. Chem.* **2012**, *124*, 2404.
[26] G. Kresse, J. Furthmüller, *Phys. Rev. B* **1996**, *54*, 11169.

